Journal of Inorganic and Organometallic Polymers and Materials (2021) 31:121–128
https://doi.org/10.1007/s10904-020-01685-5

Effect of Calcination Temperature on the Behavior of the Agglomerated Co_3O_4 Nanoparticles Obtained Through the Sol–Gel Method

L. J. Cardenas-Flechas[1] · A. M. Raba[2] · J. Barba-Ortega[3] · L. C. Moreno[4] · M. R. Joya[3]

Received: 11 May 2020 / Accepted: 20 July 2020 / Published online: 31 July 2020

Abstract
Agglomerates of Co_3O_4 were obtained using the sol–gel method for the synthesis with subsequent calcination of the samples up to 550 °C. Through X-rays it was observed that the samples presented the pure spinel phase with a crystallite size between 33.73 and 41.45 nm. In the thermogravimetric measurement from 262 °C high structural stability is presented with phase change at 917 °C. As the temperature increases, the particles increase in size, observing agglomerated nanometer particles that increase with temperature (3.5–3.8 µm). The 683 cm^{-1} Raman mode for 550 °C clearly presents an shifted compared to the other samples. The band gap for the samples under study varied with the temperature change of 1.77–1.81 eV. The *FWHM* decreases at a higher temperature, this confirms the larger crystallite size and the higher degree of sintering.

Keywords Co_3O_4 · Agglomerated · SEM · Raman

1 Introduction

Co_3O_4 is a type of metal oxide with a unique spinel structure. Within it, the Co(II) and Co(III) ions are located at the tetrahedral sites and the octahedral sites, respectively [1, 2]. This is an oxide of great interest due to its stable chemical state and its obtaining by some low-cost synthesis routes [3–5]. This material has excellent magnetic properties, transport, and optical properties. Some recent research focuses on applications in catalysis, batteries, and gas sensors [6, 7]. In nanometric size, it has been found to be efficient in electronic and optoelectronic devices [8]. Co_3O_4 has been studied in different morphologies, such as nanorods, nanosheets, nanocubes, and microstructures [9–13]. In addition, there are several synthesis methods for obtaining the Co_3O_4 material such as the hydrothermal process and sol gel, among others [14].

In recent decades, the development of nanostructures has been of great interest due to their unique properties, such as ratio of surface area, volume, increase in emissions, and optical absorption due to the transfer of electrons from one state to another [11]. A large variety of oxide compounds can be formed from metallic elements by adopting a large number of structural geometries and electronic properties that can exhibit a metallic, semiconductor, or insulator character [15–18]. In recent years, there have been several efforts to understand the optical properties of Co_3O_4. Several studies have shown that this material exhibits multiple direct band gap energies (1.482.24 eV) [16, 17].

In the literature there are several works in which the importance of Co_3O_4 in the improvement of electrodes for lithium ion batteries is observed [19–21]. These materials have been obtained in different textures and structures, however some studies report a low cyclic capacity in the elimination and absorption of lithium. Nevertheless, according to Liu et al. [21] found in their work that Co_3O_4 agglomerates favor the cycle and prolonged life of the electrodes for lithium batteries. These agglomerates the authors called secondary particles formed by primary particles. Nanoparticles,

✉ M. R. Joya
mrinconj@unal.edu.co

[1] Facultad de Ingeniería - Ciencia y Tecnología de Materiales, Universidad Nacional de Colombia, Calle 45 #30-03, Bogotá C.P. 111321, Colombia

[2] Departamento de Física, Universidad Francisco de Paula Santander, Avenida Gran Colombia # 12E-96, Cúcuta, Colombia

[3] Departamento de Física, Universidad Nacional de Colombia, Calle 45 #30-03, Bogotá C.P. 111321, Colombia

[4] Departamento de Química, Universidad Nacional de Colombia, Calle 45 #30-03, Bogotá C.P. 111321, Colombia

with their increased surface free energy, can promote sintering; however, size reduction also promotes agglomeration. In the literature applications of Co_3O_4 agglomerated material for lithium ion battery [21] possibly associated with grain limit.

The lack of more detailed research on the formation of agglomerated Co_3O_4 particles in the literature led us to carry out this work. We searched for a cheap synthesis method and, based on the calcination temperature of the samples, it was possible to control the size of the agglomerates without undergoing drastic changes in the size of the particles when calculating using X-rays (33.73–41.45 nm). The samples were calcined up to 550 °C. It was not subjected to more temperature, because we wanted the spinel phase and a certain homogeneity in composition of the material (EDS). Significant changes in Raman mode were also observed at 550 °C around $683cm^{-1}$. Through the SEM measurements it was observed that the size of the agglomerate increased with the calcination temperature. Similarly, the energy gap also increases with temperature. With the X-rays measurements it was observed that the samples were in the pure spinel phase.

2 Experimental Methods

The synthesis of Co_3O_4 was carried out through the sol–gel technique. Cobalt (II) nitrate hexahydrat ($Co(NO_3)_2 \cdot 6H_2O$)) ≥ 99%, (Merck, Germany) was used as reactant or precursor and Ethanol 96% (Merck Germany) as solvent. As precursor, 21.82 g of cobalt nitrate hexahydrate and 13.12 mL of ethanol were used as solvent. This components were mixed under continuous stirring during 23 h. A sample for thermogravimetric analysis (TGA) was taken. The gel stabilization process is started on a ramp of 0.73 °C/min up to 200 °C. The final material had a mass of 7,675 gr, subsequently the obtained resin was subjected to precalcination and calcination at different temperatures. Subsequently, the precalcining process began in an oven model Vulcan 3-1750 furnace (120V50/60Hz), programmable in multiple stages, for two hours at a temperature of 300 °C. Before calcination, the material was macerated in an agate mortar. After this process, the obtained powder was subjected to different calcination temperatures for two hours (250 °C, 350 °C, 450 °C and 550 °C).

The characterization of the samples was performed through the techniques described below. The X-ray diffraction analysis (*XRD*) was conducted on Xpert Pro Panalytical equipment with data taken at an angle of 2θ between 10° and 80°, which uses an RTMS (real time multiple strip) detector with $CuK\alpha$ radiation and a wavelength of $\lambda = 1.542$ Å and a step of 0.0263° in Brentano Bragg mode. A Cary5000 UV–Vis-NIR diffractometer was used. The UV–Vis reflectance spectrum was measured in diffuse reflectance mode in the 200–2500 nm wavelength range. With the aim of studying the optical response of the Co_3O_4 octahedron, the samples were measured with UV–visible electronic absorption spectroscopy by dispersing the particles in water (350–800 nm). The morphological analysis was performed with a FEI QUANTA 200 scanning electron microscope (SEM), in secondary electron mode at high vacuum and a voltage of 30 KV. The qualitative chemical composition analysis was performed via energy dispersion microscopy (EDS). For the Raman spectroscopy measurements, the "Thermo Scientific *DXR* Raman microscope" equipment was used, with a 532 nm excitation wavelength. For thermogravimetric measurements, the TA Instruments DSC SDT Q600 Thermogravimetric Analyzer (*TGA*) and Differential Scanning Calorimeter (*DSC*), a second generation simultaneous was used.

3 Results and Discussion

The samples obtained from the sol–gel synthesis were studied by X-ray diffraction. Figure 1, shows the XRD analysis of cobalt oxide powder obtained through calcination at temperatures of (a) 250 °C (b) 350 °C (c) 450 °C (d) 550 °C. The XRD (COD 01-074-1657) correspond to the crystallographic planes (111), (220), (311), (222), (400), (422), (511), and (440) of the spinel-like structure of Co_3O_4 with face-centered cubic (FCC), structure units of the cell, which agreed with other studies [1, 6]. The diffraction peaks were well defined, with no secondary phases for Co_3O_4. As the calcination temperature increased, there was an increase in the intensity of the *XDR* peaks, which indicates an increase in the degree of crystallization due to a tendency of minimization of the interfacial surface energy [22]. These results suggest a rapid synthesis in the formation of Co_3O_4 particles with highly pure spinel crystalline phase, using through the sol–gel method at a low cost. The samples were not subjected to higher temperatures because, according to Li et al. [23], starting a mixed phase of CoO and Co_3O_4 is obtained by the oxygen vacancies with an initial temperature at 700 ° C.

The average sizes of the particles were calculated using the Debye Scherrer equation ($0.9\lambda/(\beta cos\theta)$) to obtain the average crystallite size, λ is the wavelength, of the full width at half maximum (*FWHM*) of the diffraction peak, and θ is the Bragg angle [24]. The average size of the particles was calculated by using the most intense peak $\langle hkl \rangle$, (311). As can be seen in Table 1, the crystal size varied from 33.73 nm to 41.45 nm and increased for higher temperatures. This is comparable to data found in the literature, in which the crystal size was of 90–110 nm [25]. It is noteworthy that in this work we find particle size smaller than those reported.

The lattice parameters determined at various temperatures are given in Table 2, using the GSAS II program. The lattice

Table 1 The crystallite size calculated with the Debye-Scherrer equation

T (°C)	Peak position (2θ)	FWHM (degree)	Size (nm)
250	36.97	0.2482	33.73
350	36.95	0.2309	36.39
450	37.15	0.2210	37.90
550	36.96	0.2020	41.45

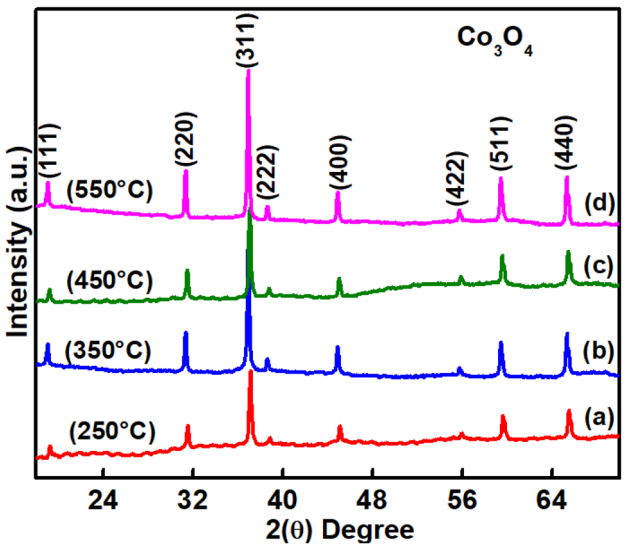

Fig. 1 X-ray spectra (XRD) for the Co_3O_4 samples obtained through the sol–gel method and calcined at different temperatures. (a) 250 °C, (b) 350 °C, (c) 450 °C and (d) 550 °C

Table 2 Lattice parameter and unit cell volume for Co_3O_4 samples at different calcination temperatures

T (°C)	a = b = c (Å)	Vol. (Å)
250	8.0535	522.341
350	8.0681	525.194
450	8.0765	526.837
550	8.0799	527.510

parameter of the cubic unit cell increases as the calcination temperature of the samples increases. Similarly, the increase in cell volume is controlled by the lattice expansion, being greater for the temperature of 550 °C (527.510 Å) and lower for 250 °C (522.341 Å).

TGA-DSC thermogravimetric measurements were carried out in a nitrogen 5% in air atmosphere with a heating rate of 10 °C/min. Figure 2 performed a TGA-DSC analysis in order to obtain information on the thermodynamic behavior of the solution precursor. In the Thermogravimetric Analysis

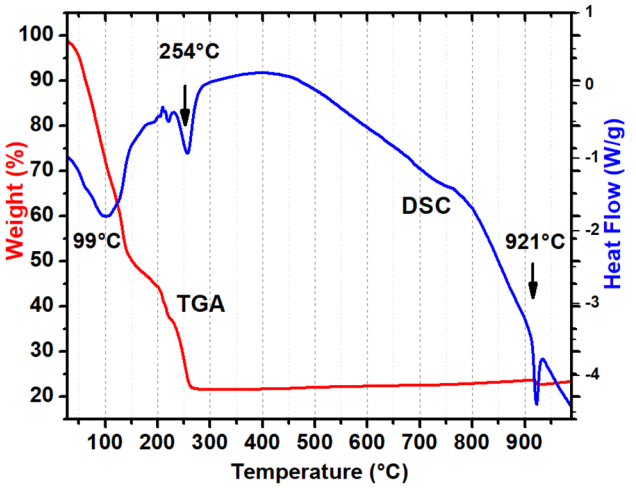

Fig. 2 TGA–DSC of the Co_3O_4 solution precursor, from room temperature to 1000 °C. The red line represents the weight change in percentage, while the blue shows the heat flow, in an atmosphere of nitrogen and air (Color figure online)

(TGA) measurement of Fig. 2, the change in weight of the sample from room temperature to 1000 °C was measured. In the TGA graph it can be seen that 45% of the weight is lost below 100 °C. This weight loss is related to the solvent. From 137 °C to 262 °C there is a 33% weight loss related to the evaporation of water molecules. In other words, a loss of up to 262 °C of solvents and nitrogen was observed. The peak at 254 °C is due to nitrogen loss due to nitrate decomposition. However, between 917 °C and 925 °C there is a weight loss of 1%, related to the phase transition of the material. From 262 °C, the samples have a high stability of the speel structure without weight loss up to 917 °C, where there is a degradation of the structure [26, 27].

In the differential scanning calorimetry (DSC) curve, the area of the peak is proportional to the enthalpy, here the endothermic peak increases when the enthalpy increases and the exothermic peak occurs in the opposite direction. The presence of a sharp endothermic peak at 99 °C also indicates an evaporation process [28, 29]. In the endothermic curve at 254 °C it is related to the reduction of $CoO(OH)$ for the spinel phase of Co_3O_4 [30] and the other endothermic curve at 921 °C is attributed to the reduction of Co_3O_4 to CoO.

The morphology and structure of the material they were characterized by means of scanning electron microscopy (SEM). Figure 3 shows SEM images of agglomerates of Co_3O_4 nanoparticles with various sizes between 3.4 and 4 µm, increasing with the calcination temperature of the samples from 250 to 550 °C. The growth of nanoparticles is closely related to the calcination temperature of the calcination. Figure 3 shows crowds with blackberry morphology with ruffled threads. Non-agglomerated nanoparticles have very high surface area to volume ratio. On the other

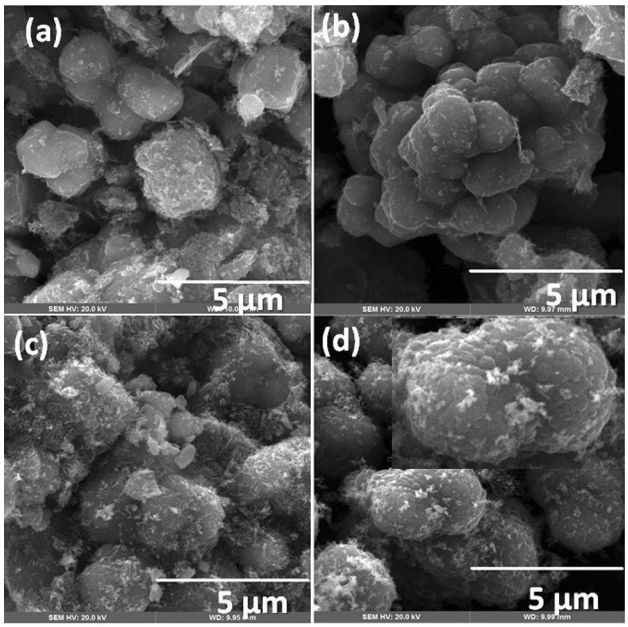

Fig. 3 SEM image of **a** 250 °C, **b** 350 °C, **c** 450 °C and **d** 550 °C of cobalt oxide

hand, the surface area in the agglomerates is small, but shows high capacity and excellent cyclical stability. Electrodes with an agglomerated Co_3O_4 structure have been shown to be advantageous compared to non-agglomerated nanoparticles [21, 31–33]. In addition, nanoparticles are said to agglomerate mainly due to the high surface energy, so due to this they tend to agglomerate to decrease this energy. By agglomerating the particles, the contact area between the particles is lost and when a material is sintered by heating, pores are closed or destroyed, in both cases, surface area is lost. Thus, there are few studies in the literature on the properties with the surface area and the specific surface area of the agglomerates of nanoparticles. In the SEM measurements of Fig. 3a–f, it is clearly revealed that the observed microstructures are in fact Co_3O_4 agglomerates with a micron order size.

In nanoparticles, the magnetic properties that are influenced by particle size and surface effects become more important as particle size decreases, due to the increase in the surface to volume ratio. Particles can be polycrystalline, single crystal, or amorphous. For example a nanoparticle with 80 nm particle size can be made of a single crystal, many subparticles with grain sizes of about 10 nm, or amorphous material [34]. In *SEM* measurements, the higher the calcination temperature, very small agglomerated nanometric particles are observed on the surface of a large particle, whose agglomerate also increases. Furthermore, when comparing with the values in Table 1, the FWHM decreases at a higher temperature, this confirms the larger crystallite size and the greater degree of sintering.

The chemical composition of the annealed oxide samples was determined through *EDS* microanalysis in the *SEM*. The results of the energy dispersive spectroscopy (EDS) analysis are observed in Fig. 4 for the sample at 350 °C. The results revealed the presence of Co, O, and C, being the most intense peak for O, followed by Co, the presence of carbon is possibly from the sample carrier tape. Similar spectra were obtained for the other samples subjected to temperature processes. For this reason this is only an example.

Table 3 shows the chemical composition of the calcined Co_3O_4 samples at different temperatures. Unlike the results in the literature after the annealing (700 °C) of the Co_3O_4 powder samples according to Li et al. [23], the material loses oxygen and changes from Co_3O_4 to CoO. According to the Table 3 on the chemical composition of the samples annealed in this research, at a temperature of 550 °C the material begins to lose oxygen.This result indicates that oxygen vacancies are being generated in the material in the spinel structure. For the sample at a temperature of 250 °C, the oxygen content is ~ 60.08% and at 550 °C it is ~ 41.44%. These results show a loss of oxygen with an increase in the calcination temperature.

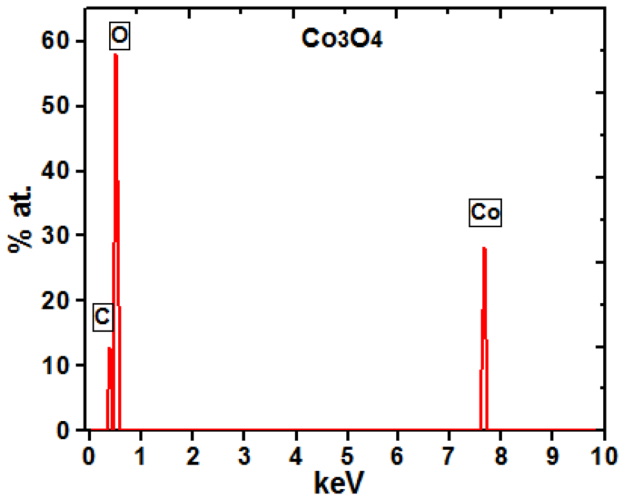

Fig. 4 Spectrum of the chemical composition for sample 350 °C–Co_3O_4 determined through EDS

Table 3 Chemical composition of the calcined Co_3O_4 samples

Temp. (°C)	% Atomic composition		
	Co	O	C
250	23.40	60.08	16.52
350	28.30	58.09	13.01
450	26.43	60.31	13.23
550	40.68	41.46	17.86

In order to observe changes in the size of the agglomerates with increasing calcination temperature ImageJ program was used for this purpose. Figure 5, shows the size of the diameter of the agglomerated particles for 250 °C, 350 °C and 450 °C; highly pure cobalt oxide powders were used. As can be seen, the agglomerated particles diameter size increases as the calcination temperature of the samples increases. In Fig. 5a, the particle size at 250 °C was (3.4 ± 05) μm, (b) at 350 °C (3.6 ± 0.1) μm, and at 450 °C (c) (3.8 ± 0.5) μm. If the size of crystallite (see Table 1) is compared with the diameter of the agglomerated particles size, see Fig. 5, it can be noted that the size is larger for higher temperatures in both cases. However, a considerable difference can be seen between the two particles and the crystallite sizes. For the agglomerated particles, the value in the diameter is higher; this indicates that the particle is composed of several Co_3O_4 crystallites, therefore, the particles (agglomerates / aggregates) are made up of many nanoparticles of the material. On the right side of Fig. 5 we have the magnification of the only agglomerate of each of the samples in which it was found in primary particle size (agglomerate).

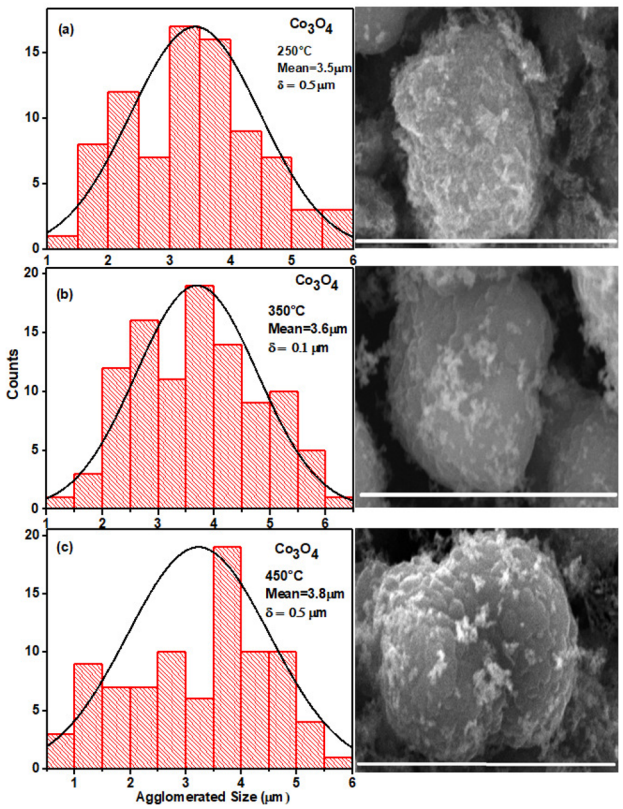

Fig. 5 Histogram of the diameter of agglomerated size: **a** 250 °C (3.5 μm, **b** 350 °C (3.6 μm), and **c** 450 °C (3.8 μm. On the right side of the figure, there is a magnification of the particle agglomerations, with a 5 μm scale bar

To observe the changes in the vibrational modes of the material under study with temperature, Raman spectroscopy was used. Figure 6 shows the typical Raman spectrum of the cobalt oxide particles annealed at 350 °C, 450 °C and 550 °C; respectively. Six active Raman modes can be noted in figure 6c, however, only five active Raman modes can be observed in Fig. 6a and b. The Raman modes for these last two, Fig. 6a and b, undergo a shift of the Raman peaks for longer wavelengths. However, for the sample calcined at 550 °C another Raman mode appears and the Raman peaks are displaced at lower wavelengths. The separation of this new peak at a temperature of 550 °C might be caused due to the oxygen defects in the crystal lattice. In the literature, for most of the Raman spectra of cobalt oxide only five active Raman modes are report [25, 35]. However, Diallo et al. [36] reported active Raman modes located at approximately $\sim 185.5, \sim 465.3, \sim 506.6, \sim 601, \sim 670,$ and $\sim 755.5\,cm^{-1}$ [36]. In the literature, it has also been found that in measurements of Raman spectroscopy CoO nanocrystals can be subjected to heating above a critical threshold of laser power and exposure time. Due to this local overheating induced by the laser itself, the Co_3O_4 phase is obtained [18]. In the samples analyzed herein, the Raman spectra were obtained with a 532 nm excitation laser, keeping the laser power.

The most intense Raman peak varies from $683.7cm^{-1}$ red-shifting and also broadening due to temperature effects and possibly due to agglomerated. Figure 6c for mode A_{1g} shows a clearly redshifted spectrum with an enlargement in the vibrational modes of its spectrum. It can be thought that the red shift is due to the increase in temperature as well as the full width half maximum (FWHM). However, in the literature it is reported that the redshift is influenced by the agglomerates of the nanoparticles [35]. Then actually

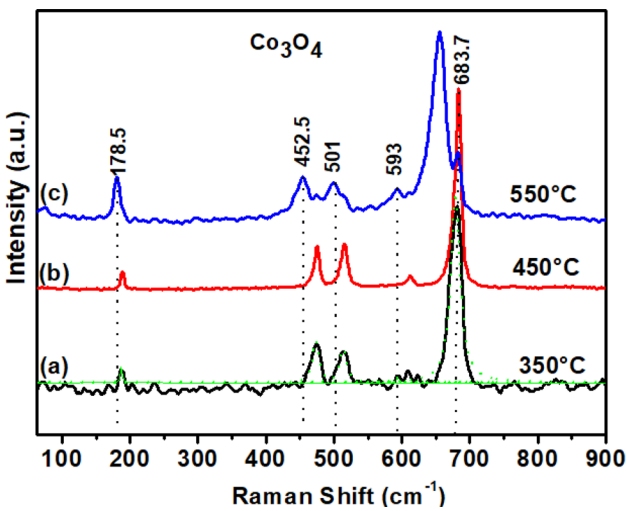

Fig. 6 Raman spectra of Co_3O_4 samples: (a) 350 °C, (b) 450 °C, and (c) 550 °C

the displacement can be a combination of the temperature and the agglomerates, which generate a phonon-phonon interaction easily transmitted between the agglomerated nanoparticles. Indicating that the agglomerations of nanoparticles alter both the production and the transmission of the phonons.

The Uv-Vis diffuse reflectance spectrum of the Co_3O_4 study samples at different annealing temperatures is shown in Fig. 7a and b. The optical properties of Co_3O_4 were studied by using of diffuse reflectance spectroscopy in the range of 250–2500 nm and are shown in Fig. 7a. In the UV- Vis spectrum, the peaks corresponding to the Co_3O_4 transitions can be observed. These transitions are crystal field $^4A_2(F) \mapsto ^4 T_1(F)$ at 1460 nm, a charge transfer $Co^{2+} \mapsto Co^{3+}$, or oxidation-reduction process at 1220 nm, as well as $O^{2-} \mapsto Co^{3+}$ at 657 nm and $O^{2-} \mapsto Co^{2+}$ nm [37]. The intensity of the peaks in UV–Vis changes with the calcination temperature of the samples, increasing for higher temperatures.

The UV–Vis spectrum of Co_3O_4 for more than one region of the spectrum permits linear extrapolation. For this reason, as far as is known in the literature, there is no agreement to date on the electronic structure of the optical absorption spectrum of Co_3O_4. Using density functional theory, Singh et al. [38] studied the optical and magnetic electronic properties of the Co_3O_4 compound. The result found for the electrical and magnetic properties of Co_3O_4, is that they are very sensitive to any change in the simulation parameters. They conclude that the fundamental band gap in Co_3O_4 is direct with a value of ca. 0.8 eV. Another article shows a fudamental band gap of 0.76 eV [23]. Furthermore, in functional PBE, [38] obtained a direct band gap of 0.34 eV at the X point of the Brillouin zone (BZ). The computed band gap is indirect ($\Gamma - X$) with values of 0.82 eV, 0.94 eV, and 0.98 eV (indirect $\Gamma - X$), 0.79 eV (direct at the X point of the BZ), respectively, according to this study. These apparent discrepancies in the band gap of cobalt oxide in the literature make it difficult to identify this material in some industrial applications. According to Drasovean et al. [39], Co_3O_4 films showed an allowed direct interband transition of 1.4–1.5 eV and 2.18–2.23 eV, respectively, while CoO films had an optical band gap energy of 2.2–2.8 eV.

Since the UV–Vis spectrum of cobalt oxide permits several extrapolations, this extrapolation is applied in two different regions (see Fig. 7b and c). Figure 7b shows the extrapolation of the spectrum in the 1.6–3.0 eV regions for the Co_3O_4 samples at the different annealing temperatures. The band gap energy of the samples varies from 1.77 to 1.81eV. However, in Fig. 7c the band gap energy varies from 0.97 to 1.02eV. The band gap is lower for lower calcination temperatures. These last results coincide with the computational results obtained by Singh et al. [38] of 0.98 eV for indirect band.

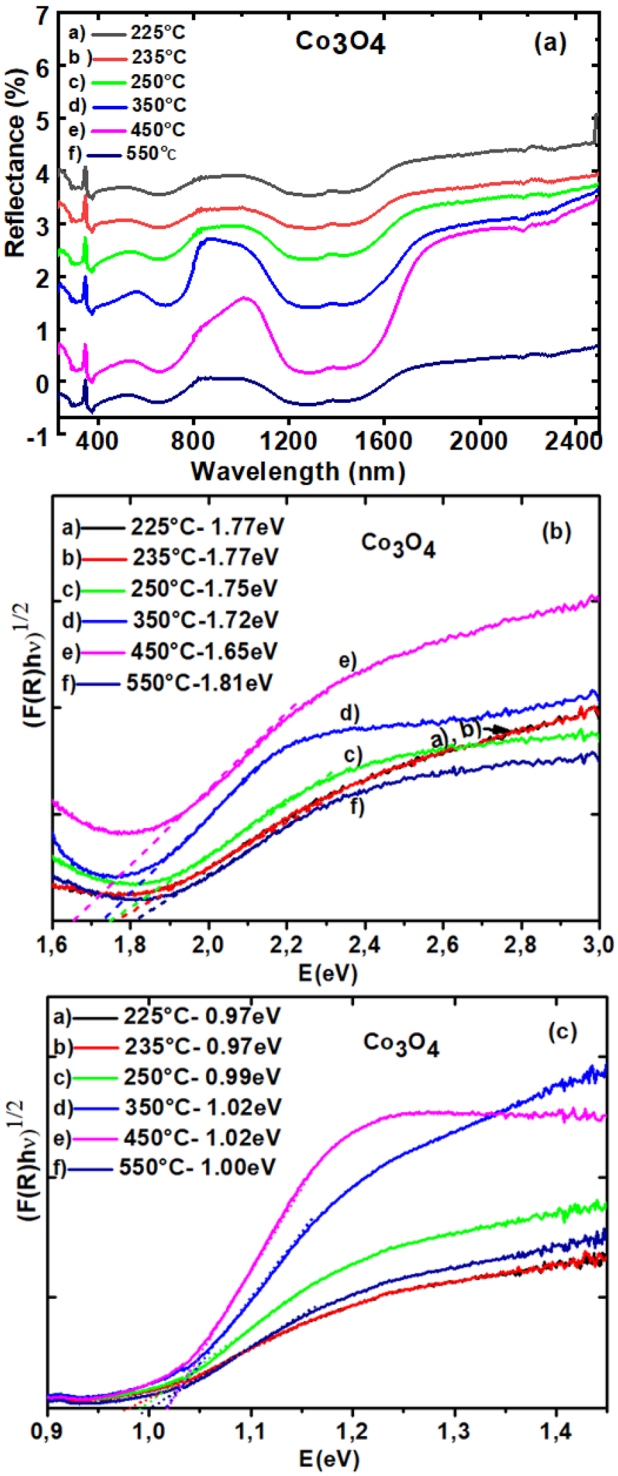

Fig. 7 **a** Reflectance (%) wavelength (nm), for the samples of Co_3O_4 at different temperatures. **b** Determination of the band gap of (a–f) for the Co_3O_4 at different temperatures for the first region of 1.6–3.0 eV. **c** Determination of the band gap of (a–f) for the Co_3O_4 at different temperatures for the second region of 0.9–1.4 eV

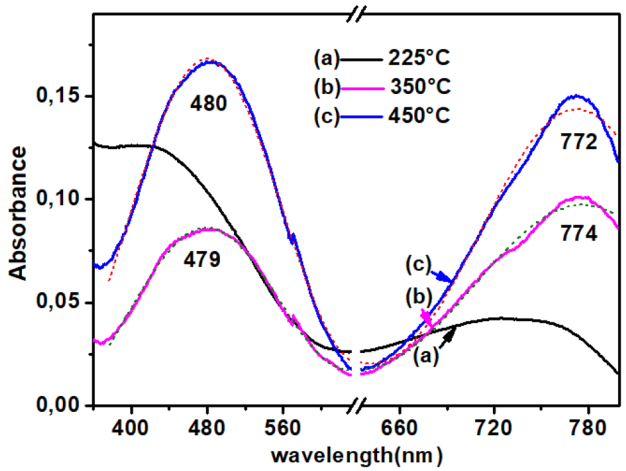

Fig. 8 UV–vis absorption spectra of synthesized particles dispersed in water

The absorption spectrum of nanoparticles Co_3O_4 in aqueous suspension is observed in figure 8. As can be seen in Fig. 8, the product shows two absorption bands in the wavelength range of 350–590 and 650–800 nm. The measurements were made for the samples at 225, 350, and 450 °C, respectively. In the first region the position of the peak changes with the calcination temperature, it is lower for lower temperatures. The peak at 480 nm can be assigned to the transition reported in the literature [40], $O^{2-}(2p) \rightarrow Co^{3+}(e_g)$ and 772 nm assigned to the transition $O^{2-} \rightarrow Co^{2+}$ [41]. The change in the position of the peak changes with the particle size. Absorption was not performed for longer wavelengths and lowered energy in order to observe the peak of 0.93 eV. Due to these transitions, the compounds showed another band edge located around 730 nm in addition to the common edge at 380 nm [42]. When the exciting light of a certain wavelength is irradiated on the compounds, the intensity of the individual luminescence peak between 400 and 550 nm decreases further. It could be said that quantum-sized Co_3O_4 in heterojunction with other compounds can induce a synergistic effect for separation and inhibit recombination of direct luminescent charge [43].The absorption band near 770 nm is also related to the $O^{2-} \rightarrow Co^{3+}$ charge transfer in this p-type semiconductor. As can be seen in Fig. 8 as the calcination temperature and the size of agglomerated particles increases, the absorption is greater.

4 Conclusions

With the sol–gel synthesis route, we obtained agglomerated Co_3O_4 nano-sized particles with diameters of around 3.8μm. The samples with increasing temperature did not present secondary phases, only the spinel phase. Through thermogravimetric measurements we observe that the material presents a structural phase change at 917 °C. The band gap is lower for lower calcination temperatures. The maximum calcination temperature for the samples was 550 °C. In the EDS and Raman measurements, significant changes in oxygen content and changes in the spectrum were observed for the temperature of 550 °C. By agglomerating the particles due to high surface energy, the surface area is lost. However, controlling the agglomerated structure with various primary particle sizes can use some applications. Agglomeration or sintering of the material eliminates grain boundary defects and we believe that it improves the processes associated with conductivity.

Acknowledgements The authors acknowledge the support of Universidad Nacional de Colombia in Bogotá. Edwin Murillo professor at Universidad Francisco de Paula Santander in Cúcuta, Colombia, for the laboratory.

Compliance with Ethical Standards

Conflict of interest The authors certify that they have not signed an agreement with any sponsor of the research reported.

References

1. P. Yang, F. Wu, L. Wang, X. Chen, J. Xie, Nanostructuring Co_3O_4 to tune capacitive behaviors: from low to high dimensions. Chem. Select. **5**, 3638–3643 (2020)
2. L. Cardenas, A. Raba, R.M. Joya, Synthesis and evaluation of nickel doped Co_3O_4 produced through hydrothermal technique. Dynamics **87**, 184–191 (2020)
3. H. Sahan, H. Goktepe, S. Yildiz, C. Caymaz, S. Patat, A novel and green synthesis of mixed phase CoO@Co3O4@C anode material for lithium ion batteries. Ionics **25**, 447–455 (2019)
4. R.M. Kakhki, M. Bina, Dispersive micro-solid phase extraction based on Co_3O_4 modified nanoclinoptilolite for fast determination of malachite green in the environmental water samples. J. Inorg. Organomet. Polym. **30**, 2475–2479 (2020)
5. M. Li, C. Han, Y. Zhang, X. Bo, L. Guo, Facile synthesis of ultrafine Co_3O_4 nanocrystals embedded carbon matrices with specific skeletal structures as efficient non-enzymatic glucose sensors. Anal. Chim. Acta **861**, 25–35 (2015)
6. J. Cao, S. Wang, X. Zhao, Y. Xing, J. Li, D. Li, Facile synthesis and enhanced toluene gas sensing performances of Co_3O_4 hollow nanosheets. Mater. Lett. **263**, 127215 (2020)
7. R. Kumar, $NiCo_3O_4$ nano-/microstructures as high-performance biosensors: a review. Nano-Micro Lett. **12–122**, 1–52 (2020)
8. M.M. Abdullah, M.S. Akhtar, S.M. Al-Abbas, Facile growth and promising applications of cobalt oxide (Co_3O_4) nanoparticles as chemi-sensor and dielectric material. Curr. Nanosci. **14**, 343–351 (2018)
9. K. Choi, H. Kim, K.M. Kim, D.W. Liu, G.Z. Cao, J.H. Le, C_2H_5OH sensing characteristics of various Co_3O_4 nanostructures prepared by solve thermal reaction. Sensors Actuators B **146**, 183–189 (2010)

10. B. Zhang, X. Zhou, C. Jiang, F. Qu, M. Yang, Facile synthesis of mesoporous Co_3O_4 nanofans as gas sensing materials for selective detection of xylene vapor. Mater. Lett. **128**, 127–130 (2018)
11. C. Yan, Y. Zhu, Y. Li, Z. Fang, L. Peng, X. Zhou, G. Yu, Built-in electric field enabled in carbon-doped Co_3O_4 nanocrystals for superior lithium-ion storage. Adv. Funct. Mater. **28**, 1705951 (2018)
12. S.L. Zhang, B.Y. Guan, X.F. Lu, S. Xi, Y. Du, X.W.D. Lou, Metal atom-doped Co_3O_4 hierarchical nanoplates for electrocatalytic oxygen evolution***. Adv. Mater. **1000**, 10000 (2020). https://doi.org/10.1002/adma.20200223
13. X. Xie, C. Ni, Z. Lin, D. Wu, X. Sun, Y. Zhang, W. Du, Phase and morphology evolution of high dielectric CoO/Co_3O_4 particles with Co_3O_4 nanoneedles on surface for excellent microwave absorption application. Chem. Eng. J. **396**, 125205 (2020)
14. T. He, D. Chen, X. Jiao, Controlled synthesis of Co_3O_4 nanoparticles through oriented aggregation. Chem. Mater. **16**, 737–743 (2004)
15. B. Raghavendra, T. Sankarappa, A. Malge, Structural, optical absorption and conductivity of PIn/Co_3O_4 composites******. J. Inorg. Organomet. Polym. **10000**, 10000 (2020). https://doi.org/10.1007/s10904-020-01589-4
16. A. Lakehal, B. Bedhiaf, A. Bouaza, H. Benhebal, A. Ammari, C. Dalache, Structural, optical and electrical properties of Ni-doped Co_3O_4 prepared via sol–gel technique. Mater. Res. **21**, 1–8 (2018)
17. L. Qiao, H.Y. Xiao, H.M. Meyer, J.N. Sun, C.M. Rouleau, A.A. Puretzky, M.D. Biegalski, Nature of the band gap and origin of the electro-/photo-activity of Co_3O_4. J. Mater. Chem. C. **1**, 4628 (2013)
18. W. Shi, F. Guo, C. Zhu, H. Wang, H. Li, H. Huang, Y. Liu, Z. Kang, Carbon dots anchored on octahedral CoO as a stable visible-light-responsive composite photocatalyst for overall water splitting. J. Mater. Chem. A **5**, 19800 (2017)
19. L. Chao, C. Taiqiang, X. Weijing, L. Xiaobing, P. Likun, C. Qun, H. Bingwen, Mesoporous nanostructured Co_3O_4 derived from MOF template: a high-performance anode material for lithium-ion batteries. J. Mater. Chem. A **3**, 5585–5591 (2015)
20. S. Jinxiao, Z. Hu, Z. Meizhou, F. Jianhui, Y. Aihua, Facile synthesis of metal-organic framework-derived Co_3O_4 with different morphologies coated graphene foam as integrated anodes for lithium-ion. J. Alloys Compd. **768**, 1049–1057 (2018)
21. B. Liu, X. Zhang, H. Shioyama, T. Mukai, T. Sakai, Q. Xu, Converting cobalt oxide subunits in cobalt metal-organic framework into agglomerated Co_3O_4 nanoparticles as an electrode material for lithium ion battery. J. Power Sources **195**, 857861 (2010)
22. R. Gao, Z. Yang, L. Zheng, L. Gu, L. Liu, Y. Lee, Z. Hu, X. Liu, Enhancing the catalytic activity of Co_3O_4 for LiO_2 batteries through the synergy of surface/interface/doping engineering. ACS Catal. **8**, 1955 (2018)
23. Y. Li, W. Qiu, F. Qin, H. Fang, V.G. Hadjiev, D. Litvinov, J. Bao, Identification of cobalt oxides with Raman scattering and Fourier transform infrared spectroscopy. J. Phys. Chem. C. **120**, 4511–4516 (2016)
24. A. Raba, J. BarbaOrtega, M. Joya, Effects of metal doping agent on the properties of $Nb_{2-x}M_xO_5$ (M = Mn, Fe, and Ni) system. Int. J. Appl. Ceram. Technol. **15**, 1577–1583 (2018)
25. J. Jiang, L. Li, Synthesis of sphere-like Co_3O_4 nanocrystals via a simple polyol route. Mater. Lett. **61**, 4894–4896 (2007)
26. R. Tummala, R.K. Guduru, P.S. Mohanty, Nanostructured Co_3O_4 electrodes for supercapacitor applications from plasma spray technique. J. Power Sources **209**, 44–51 (2012)
27. R. Tummala, R.K. Guduru, P.S. Mohanty, Binder free, porous and nanostructured Co_3O_4 anode for Li-ion batteries from solution precursor plasma deposition. J. Power Sources **199**, 270–277 (2012)
28. Y. Mussa, F. Ahmed, M. Arsalan, E. Alsharaeh, Two dimensional (2D) reduced graphene oxide (RGO)/hexagonal boron nitride (h-BN) based nanocomposites as anodes for high temperature rechargeable lithium-ion batteries. Sci. Rep. **10**, 1882 (2020)
29. R. Itteboina, T.K. Sau, Sol–gel synthesis and characterizations of morphology-controlled Co_3O_4 particles. Mater. Today. Proc. **9**, 458467 (2019)
30. B. Tomić-Tucaković, D. Majstorovic, D. Jelic, S. Mentus, Thermogravimetric study of the kinetics of Co_3O_4 reduction by hydrogen. Thermochim. Acta. **541**, 15–24 (2012)
31. X. Deng, Z. Huang, W. Wang, R.N. Dav, Investigation of nanoparticle agglomerates properties using Monte Carlo simulations. Adv. Powder Technol. **27**, 19711979 (2016)
32. A.M. Tonelli, J. Venturini, S. Arcaro, J.G. Henn, D.J. Moura, A.D.C. Viegas, C.P. Bergmann, Novel coreshell nanocomposites based on TiO_2 covered magnetic Co_3O_4 for biomedical applications. J. Biomed. Mater. Res. Part B Appl. Biomater. **108**, 1879–1887 (2020)
33. A. Takafumi, I. Toshio, M. Yoshitake, S. Woosuck, M. Ichiro, K. Masahito, Gas sensor properties of nanopore-bearing Co_3O_4 particles containing Pt or Pd particles. J. Asian Ceram. Soc. **8**(1), 138–148 (2020)
34. D. Trpkov, M. Panjan, L. Kopanja, M. Tadi, Hydrothermal synthesis, morphology, magnetic properties and self-assembly of hierarchical $\alpha - Fe_2O_3$ (hematite) mushroom-, cube-and sphere-like superstructures. Appl. Surf. Sci. **457**, 427–438 (2018)
35. I. Lorite, J.J. Romero, J.F. Fernndez, Effects of the agglomeration state on the Raman properties of Co_3O_4 nanoparticles. J. Raman Spectrosc. **43**, 14431448 (2012)
36. A. Diallo, A.C. Beye, T.B. Doyle, E. Park, M. Maaza, Green synthesis of Co_3O_4 nanoparticles via *Aspalathus linearis*: physical properties. Green Chem. Lett. Rev. **8**, 30–36 (2015)
37. G. George, S. Anandhan, A comparative study on the physicochemical properties of sol–gel electrospun cobalt oxide nanofibres from two different polymeric binders. RSC Adv. **5**, 81429–81437 (2015)
38. V. Singh, M. Kosa, K. Majhi, D.T. Major, Putting DFT to the test: a first-principles study of electronic, magnetic, and optical properties of Co_3O_4. J. Chem. Theory Comput. **11**, 64–72 (2014)
39. R. Drasovean, S. Condurache-Bota, Structural characterization and optical properties of Co_3O_4 and CoO films. J. Optoelectron. Adv. Mater. **11**, 2141 (2009)
40. C.M. Jiang, L.R. Baker, J.M. Lucas, J. Vura-Weis, A.P. Alivisatos, S.R. Leone, Characterization of photo-induced charge transfer and hot carrier relaxation pathways in spinel cobalt oxide (Co_3O_4). J. Phys. Chem. C. **118**, 22774–22784 (2014)
41. A.K. Sarfraz, S.K. Hasanain, Size dependence of magnetic and optical properties of Co_3O_4 nanoparticles. Act. Phys. Pol. A. **125**, 139–144 (2014)
42. J. Pal, P. Chauhan, Study of physical properties of cobalt oxide (Co_3O_4) nanocrystals. Mater. Charact. **61**, 575–579 (2010)
43. H. Zhang, W. Tian, L. Zhou, H. Sun, M. Tade, S. Wang, Monodisperse Co_3O_4 quantum dots on porous carbon nitride nanosheets for enhanced visible-light-driven water oxidation. Appl. Catal. B Environ. **223**, 2–9 (2018)